Trends in synchrotron-based tomographic imaging: the SLS experience

M. Stampanoni, A. Groso, A. Isenegger, G. Mikuljan, Q. Chen, et al.

M. Stampanoni, A. Groso, A. Isenegger, G. Mikuljan, Q. Chen, A. Bertrand, S. Henein, R. Betemps, U. Frommherz, P. Böhler, D. Meister, M. Lange, R. Abela, "Trends in synchrotron-based tomographic imaging: the SLS experience," Proc. SPIE 6318, Developments in X-Ray Tomography V, 63180M (7 September 2006); doi: 10.1117/12.679497

SPIE.

Event: SPIE Optics + Photonics, 2006, San Diego, California, United States

Invited Paper

Trends in synchrotron-based tomographic imaging: the SLS experience

M. Stampanoni, A. Groso, A. Isenegger, G. Mikuljan, Q. Chen, A. Bertrand, S. Henein, R. Betemps, U. Frommherz, P. Böhler, D. Meister, M. Lange and R. Abela

Swiss Light Source, Paul Scherrer Institut, CH-5232 Villigen, Switzerland

ABSTRACT

Synchrotron-based X-ray Tomographic Microscopy (SRXTM) is nowadays a powerful technique for non-destructive, high-resolution investigations of a broad kind of materials. High-brilliance and high-coherence third generation synchrotron radiation facilities allow micrometer and sub-micrometer, quantitative, three-dimensional imaging within very short time and extend the traditional absorption imaging technique to edge-enhanced and phase-sensitive measurements. At the Swiss Light Source TOMCAT, a new beamline for TOmographic Microscopy and Coherent rAdiology experimenTs, has been recently built and started regular user operation in June 2006. The new beamline get photons from a 2.9 T superbend with a critical energy of 11.1 keV. This makes energies above 20 keV easily accessible. To guarantee the best beam quality (stability and homogeneity), the number of optical elements has been kept to a minimum. A Double Crystal Multilayer Monochromator (DCMM) covers an energy range between 8 and 45 keV with a bandwidth of a few percent down to 10^{-4}. The beamline can also be operated in white-beam mode, providing the ideal conditions for real-time coherent radiology. This article presents the beamline design, its optical components and the endstation. It further illustrates two recently developed phase contrast techniques and finally gives an overview of recent research topics which make intense use of SRXTM.

Keywords: X-ray imaging, synchrotron microtomography, multilayer monochromator, coherent radiology

1. INTRODUCTION

The combination of X-ray microscopy with tomographic techniques as well as the exceptional properties of third-generation synchrotron radiation sources allow to obtain volumetric information of a specimen at micron or sub-micron scale with minimal sample preparation. In addition, the coherent nature of synchrotron radiation extends the classical absorption based tomography towards edge-enhanced and phase-contrast investigations. Requirements on the beamline components (beam intensity, size, stability, homogeneity) and detectors (resolution, efficiency, speed and noise) are very high and tremendous efforts have been made all over the world to develop high performance synchrotron-based microtomography devices. Sect. 2 presents some technical aspects of TOMCAT, the novel beamline for TOmographic Microscopy and Coherent rAdiology experimenTs, at the Swiss Light Source (SLS). Even though almost the totality of today's routine users perform absorption-based or "edge-enhanced" tomography experiments, see Sect. 4, there is a growing interest on phase contrast imaging. The advantages of X-ray phase contrast radiography over conventional radiography are evident. First, the phase shift of light absorbing materials can be sufficiently big to be detected with phase-sensitive methods and, second, phase signals are produced with much lower dose deposition than absorption, which can be very important when radiation damage becomes an issue. It has been shown that interferometric techniques as proposed by Bonse and Hart,[1] or phase retrieval methods[2] work fine but are somehow difficult to use in a routine experiment because of their complexity (stability and alignment issues for the first one, data processing for the second one). Recently, see Sect. 3, two new methods have been introduced which set a novel approach to the phase contrast problem: the Differential Phase Contrast (DPC) technique[3] and the Modified Bronnikov Algorithm (MBA).[4,5] The DPC is based on a combination of grid-interferometry and phase stepping and is particularly suited for large objects and when a moderate resolution is required. The MBA is based on fast and direct 3D approach and works perfectly when micrometer resolution is necessary and the samples are small. It appears clear that the development potential of micron- and submicron tomography applications, in absorption or in phase, is far to be accomplished: the SLS and its TOMCAT beamline will be at the forefront in this context.

Send correspondence to Marco Stampanoni, E-mail: marco.stampanoni@psi.ch, Telephone: +41 56 310 47 24

Developments in X-Ray Tomography V, edited by Ulrich Bonse,
Proc. of SPIE Vol. 6318, 63180M, (2006) · 1605-7422/06/$15 · doi: 10.1117/12.679497

2. TOMCAT: A BEAMLINE FOR TOMOGRAPHIC MICROSCOPY AND COHERENT RADIOLOGY EXPERIMENTS

The TOMCAT beamline is located at the X02DA port of the SLS and started regular user operation in June 2006. Synchrotron light is delivered by a 2.9 T superbend: compared with the 1.4 T of the normal SLS bending magnets this shifts the critical energy of the source from 5.4 keV up to 11.1 keV resulting in a considerable increase of flux at hard X-rays (> 20 keV), see Figure 1.

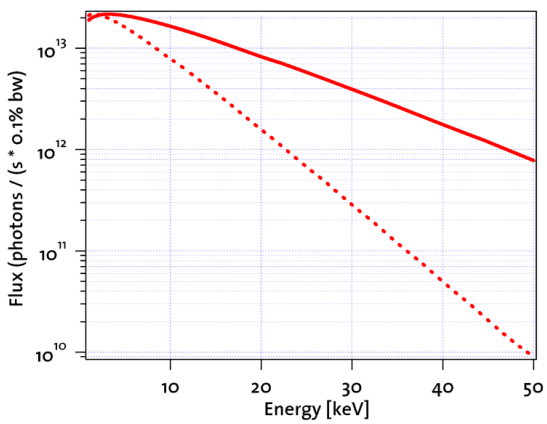

Machine Parameters	
Ring energy	2.4 GeV
Ring current	400 mA
Source parameters	
Magnetic field	2.9 T
Critical energy	11.1 keV / 1.12 Å
Electron source size (σ_x, σ_y)	46 μm, 16 μm
Electron source divergence (σ'_x, σ'_y)	109 μrad,16 μrad
Photon source size (Σ_x, Σ_y)	53 μm, 16 μm
Photon source divergence (Σ'_x, Σ'_y)	2 mrad, 0.6 mrad

Figure 1. Left: estimated photon flux (vertical integrated and 2 mrad horizontal acceptance) for the 2.9 T superbend (full line) and for the 1.4 T normal bend (dashed line). The gain in flux at energies above 20 keV is evident. Right: Relevant parameters of the source. The vertical divergence is, of course, energy dependent. The value of 0.6 mrad corresponds to the acceptance of the beamline diaphragm.

2.1. Design and realization

Rationale: Real space, full field imaging, and in particular tomography, needs a homogeneous and stable beam profile, in order to perform optimal background corrections. Because of the high coherence of the radiation produced by third-generation synchrotron radiation facilities like the SLS, all the optical components (windows, mirrors and monochromator) must be designed with particular care in order to avoid deterioration of the beam profile. The design criteria for the optics of the TOMCAT beamline have been:

- Keep the optics as simple as possible (i.e. minimize the number of optical elements)
- Optimize optics for bandwidth rather than for energy resolution
- Monochromatic beam and white beam must be available
- Energy range: 6-45 keV

Window: The machine UHV-sector (10^{-10} mbar) is separated from the beamline HV (10^{-7} mbar) by a Chemical Vapour Deposited (CVD) diamond window, see Figure 3b. Because of their better surface-roughness, CVD diamond windows are preferred to standard Be-windows. The thickness of the window is 100 μm and its surface-roughness 2.5 nm RMS. Coherence degradation due to the window has been measured with shearing interferometry[6] and resulted to be negligible.

Optics The main optical component of the TOMCAT beamline is a fixed-exit double crystal multilayer monochromator (DCMM) which covers an energy range from 6 to 45 keV. Design and manufacturing have been done by CINEL Strumenti Scientifici, Padova, Italy. The DCMM is located in the front-end, at approximately 7 m from the source: this allows to accept a large angular divergence while keeping the optical elements

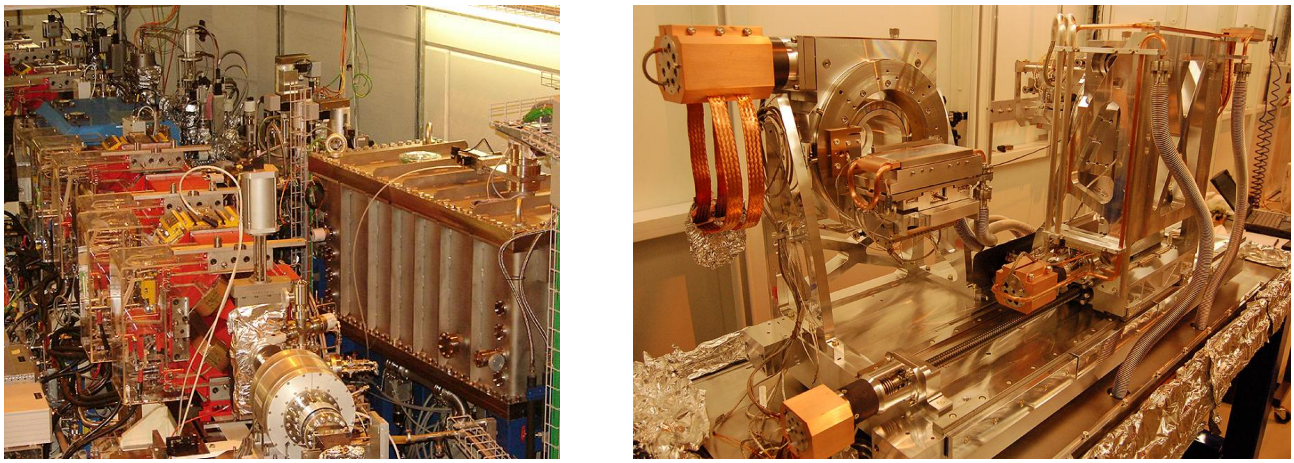

Figure 2. Left: View of the sector 2 of the SLS tunnel: visible are the magnets of the storage ring (in the foreground) as well as the TOMCAT's front end (background). The monochromator vacuum chamber is clearly visible on the right side. Right: View of the mechanics of the mono: the multilayer crystals are mounted on two separate goniometer towers. The first crystal can be adjustd in transversal direction as well as pitch and roll. The second crystal has transversal, longitudinal (up to 850 mm range), vertical as well as pitch, roll and yaw adjustment. Both crystals are supported by a bank which is vertical translated and tilted by three jacks.

very compact, see Fig. 2. $[Ru/C]_{100}$ and a $[W/Si]_{100}$ multilayer stripes have been coated 8 mm apart from each other on a Si111 substrate (active area of 150x50 mm^2), see Fig. 3c. As a result the energy bandwidth of the DCMM is a few percent when multilayer are used or 10^{-4} when the silicon is used. The slope errors figures in the direction along and across the optic are better than 0.5 μrad RMS and 5 μrad RMS respectively. Surface roughness is less than 0.3 nm RMS. When operating with multilayers the Bragg angle varies between $\theta_B = 1.82°$ and $\theta_B = 0.265°$ for energies ranging from 5 keV up to 45 keV. For the low-energy settings, the power density is 80 mW/mm^2 and is dissipated via a water side-cooling. The crystal optics are mounted on two independent high-precision goniometers. The first crystal has motorized pitch, roll, and horizontal translation (for stripes selection); the second crystal has the same degrees of freedom and, in addition, yaw and vertical translation. The whole system is positioned on a base plate that can be vertically adjusted. The distance between both crystals can be increased up to 850 mm. Instead of using a collimating mirror, the vertical size of the beam is "controlled" by moving the endstation along the beam path (up to 15 m travel range).

Sample manipulator The sample manipulator has been designed and manufactured at PSI. Translation along all the three space direction is performed with a resolution better than 1 micron. The axis perpendicular to the beam direction has a reproducibility of 0.1 micron: this is imperative for an artefact-free acquisition of reference images. The sample can be centered also with 0.1 micron reproducibility. The rotation axis is air-bearing based and has a run-out error of less then 1 micron at 100 mm from the rotation surface. The whole system can be swapped by 90°, see Figure 3d, allowing to scan thick and short sample (vertical rotation axis) or long and thin samples (horizontal rotation axis).

Detector The most established detection method consists of converting X-rays into visible light with a scintillator and projecting them onto a charge coupled device (CCD) with the help of suitable optics.[7–10] This approach provides reliable and reproducible results for a wide range of research fields covering both medicine and biology[11–14] as well as materials science.[15–17] The TOMCAT detector follows the same principle: with interchangeable (motorized) objectives the field of view can easily be varied from 0.75x0.75 mm^2 up to 11.45x11.45 mm^2 with pixel sizes ranging from 0.35x0.35 μm^2 up to 5.6x5.6 μm^2. The CCD camera has 2048x2048 pixels (7x7 μm^2 pitch) and a full frame is read-out in 260 ms with nominal 14 bits. Readout noise is 9 e$^-$ at 10 MHz and 12 e$^-$ at

20 MHz, dark current is 0.022 e^-/ s/pixel. Table 1 summarizes the several imaging option (field of view and pixel size) available.

Table 1. Specifications of the different objectives available for the microscope

Objective	Magnification	NA	Field of View (mm^2)	Pixel Size (μm^2)	Interp. Pixel Size (μm^2)*
PLAPO1.25x	1.25	0.06	11.4 x 11.4	5.6 x 5.6	2.8 x 2.8
PLAPO2x	2	0.08	7.15 x 7.15	3.50 x 3.50	1.75 x 1.75
UPLAPO4x	4	0.16	3.58 x 3.58	1.75 x 1.75	0.88 x 0.88
UPLAPO10x	10	0.40	1.43 x 1.43	0.70 x 0.70	0.35 x 0.35
UPLAPO20x	20	0.70	0.72 x 0.72	0.35 x 0.35	0.18 x 0.18
UPLAPO40x	40	0.85	0.36 x 0.36	0.18 x 0.18	0.09 x 0.09

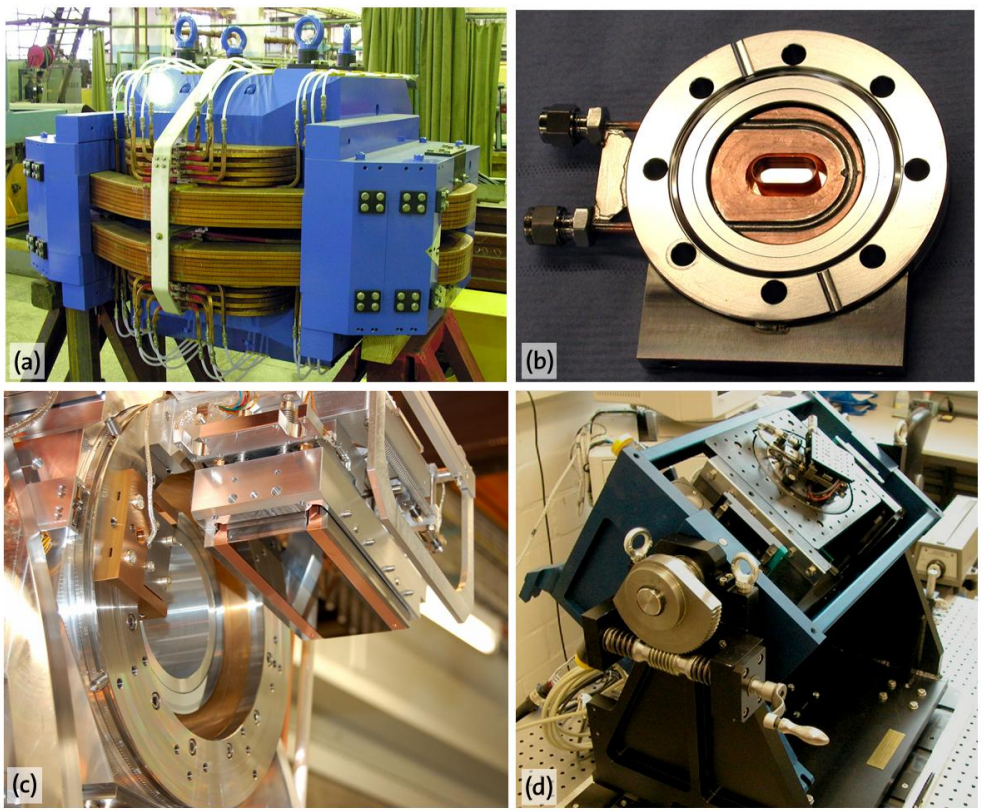

Figure 3. (a) The 2.9 T superbend before the installation in the ring. (b) The CVD window installed in the front end: clearly visible is the copper frame, which is water cooled. (c) Multilayer crystals installed on one goniometer of the TOMCAT monochromator. Visible are the three ($[Ru/C]_{100}$, $[W/Si]_{100}$ and Si111) regions on the substrate. (d) The sample manipulator "frozen" during the axis swapping procedure.

3. NOVEL APPROACHES TO PHASE CONTRAST IMAGING

Absorption based X-ray radiographic imaging is an invaluable standard tool, used routinely for non-destructive investigations in medicine, biology or environmental and materials science. For important samples as biological tissue, polymers, or fiber composites, however, the use of conventional X-ray radiography is limited because

*The CCD camera has an hardware interpolation feature, which allows to "double" the resolution of the chip.

these objects show only weak absorption contrast. On the other hand, the cross section for elastic scattering of hard X rays in matter, which causes a phase shift of the wave passing through the object of interest, is usually much greater than that for absorption. Therefore, recording the X-ray phase shift instead of the absorption substantially increases the contrast. As a consequence, several phase-sensitive X-ray imaging methods have been developed in the past years. They can be classified into interferometric methods,[1,18] techniques using an analyzer crystal,[19,20] and free-space propagation methods.[2,21] These techniques are different in terms of experimental setup, requirements in the illuminating radiation and the nature of the detected signal. We introduce here two solutions that overcome most of the limitations of the previous methods. In section 3.1 we present the so-called *differential phase contrast imaging* method, which is particulary suited when moderate spatial resolution and large field of view are needed. In section 3.2 we describe a *full 3D phase imaging* method, which is very well suited when high spatial resolution and speed are required.

3.1. Differential Phase Contrast (DPC) imaging with grating interferometry

The use of gratings as optical elements in hard X-ray phase imaging can overcome some problems that so far impair the wider use of phase contrast in X-ray radiography and tomography. Weitkamp *et. al*[3] experimentally realized an hard X-rays grating interferometer originally proposed by David *et. al.*[22]

3.1.1. Theoretical background

The functional principle of the grating interferometer is depicted in Figure 4.

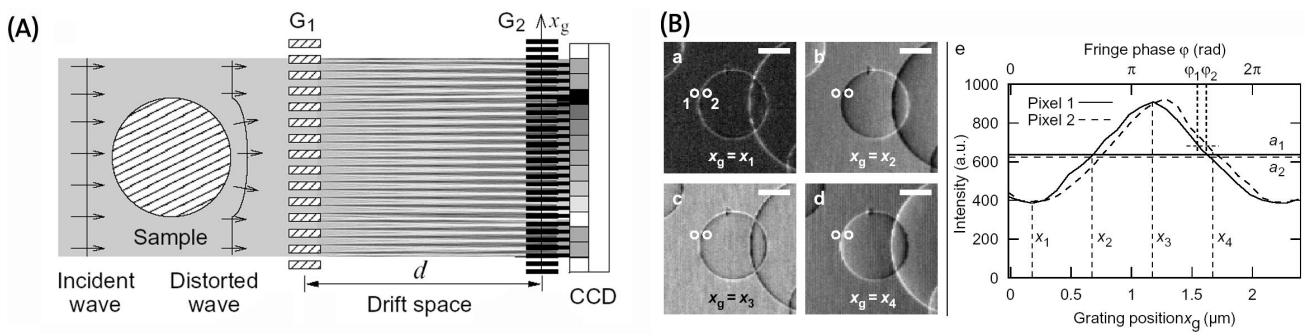

Figure 4. (A) Functional principle of the grating interferometer, details see text. (B) Principle of phase stepping: (a-d) interferograms of polystyrene spheres (100 and 200 μm diameter) taken at different relative position $x_g = x_1, ..., x_4$. (e) Intensity oscillation in two different detector pixels $i = 1, 2$ as a function of x_g. For each pixel, the oscillation phase ϕ_i and the average intensity a_i over one grating period can be determined, see Ref. [3]. Scale bar 50 microns.

A beamsplitter grating G_1 essentially divides the incident beam into the two first diffraction orders. Since the wavelength λ of the illuminating hard X-rays ($\approx$ 1 Å) is much smaller than the grating pitch ($\approx$ 1 μm), the angle between the two diffracted beams is so small that they overlap almost completely. Downstream of the beam-splitter grating, the diffracted beams interfere and, when illuminated with a plane or spherical wave, form linear periodic fringe patterns in planes perpendicular to the optical axis. The idea is to detect the positions of the fringes and determine from these the shape of the wave front. However, since the pitch of the phase grating (and thus the spacing of the interference fringes) does not exceed a few microns, an area detector placed in the detection plane will generally not have sufficient resolution to resolve the fringes, and the exact position of their maxima. Therefore, an absorbing grating G_2 with the same periodicity and orientation as the fringes is placed in the detection plane, just in front of the detector. This analyzer grating acts as a transmission mask for the detector and transforms the local fringe position into signal intensity variation. The recorded signal contains therefore quantitative information about the *phase gradient* of the object. To separate this phase information from other contributions to the signal, such as absorption in the sample, inhomogeneous illumination or imperfections of the gratings, the phase-stepping approach used in visible-light interferometry was adapted to this setup, see Figure 4(B) and Ref. [23]. The phases $\varphi(x, y)$ of the intensity oscillations in each pixel are related to the wave-front phase profile $\Phi(x, y)$, the X-ray wavelength λ, the distance d between the two gratings,

and the period g_2 of the absorption grating by the expression $\varphi = \frac{\lambda d}{g_2}\frac{\partial \Phi}{\partial x}$. The quantity φ contains no other contributions, particularly no absorption contrast. The phase profile Φ of the object can thus be obtained from $\varphi(x, y)$ by a simple one-dimensional integration.[3]

3.1.2. Experimental results

The grating interferometer is mechanically very robust, requires little spatial coherence, is polychromatic, quantitative and scalable up to large field of views. Figure 5 shows the capability of the interferometer in imaging biological samples. A rat heart placed in a plastic container filled with water (4% formalin) was imaged at an X-ray wavelength of 0.69 Å. Two images are stitched together from two frames of 15mm x 15mm, the spacial resolution was 7.5 microns. The grating periods were $p_1 = 4$ μm and $p_2 = 2$ μm, the grating distance was $d = 175$ mm. The absorption image (a) shows poor contrast (few percent) mainly due to the lower absorption of fatty tissue near the upper end of the sample. On the other hand the phase gradient image (b) shows strongly enhanced contrast revealing a variety of details. The phase image (c) is obtained by numerical integration of the gradient image and phase shifts of up to 8π are measured. The dose applied to the sample with the differential

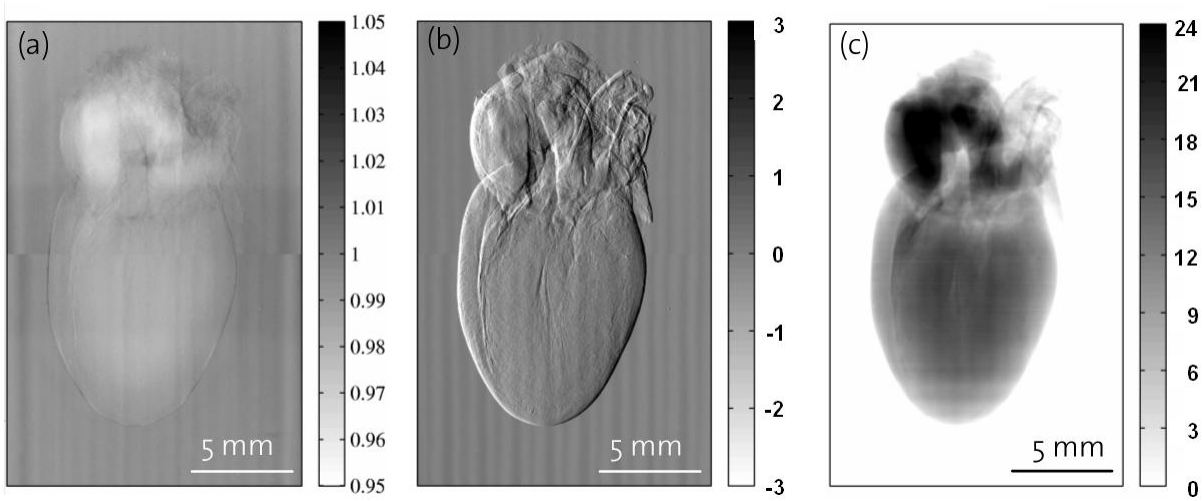

Figure 5. Image of a rat heart in formalin solution. (a) absorption, (b) phase gradient and (c) phase image. Data have been acquired at ID19 of the ESRF. Images courtesy of F. Pfeiffer, PSI.

phase contrast technique scales with the number of phase steps needed. This number is equal to 3 for a perfect sinusoidal curve. For the sample described in Fig. 5, the number of required steps was 8, so eight times more dose has been deposited in the sample compared to classical absorption tomography. On the other hand, the enormous gain obtained in terms of contrast sufficiently balances the additional irradiation.

3.2. Full 3D phase imaging technique

The methods used so far for phase tomography (quantitative volumetric reconstruction of the refractive index), either interferometric or not, are based on a two step approach: first, the projections of the phase are determined in the form of Radon projections (phase retrieval) and then the object function, i.e. the refractive index decrement δ is reconstructed applying a conventional filtered backprojection algorithm. As an alternative, Bronnikov suggested an algorithm which eliminates the intermediate step of 2D phase retrieval and provides a *direct* 3D reconstruction of the refractive index of the object.[24,25] Since far from absorption edges δ is linearly related to the electron density ρ, which is - except for hydrogen rich materials - proportional to the mass density, the resulting reconstruction represents approximately the distribution of the mass density in the sample.

3.2.1. Theoretical background

Let consider a monochromatic plane wave with wavelength λ that propagates along the positive z-axis and that impinges upon a thin mixed phase-amplitude object, which is characterized by the linear absorption coefficient

$\mu(x_1, x_2, x_3)$ and the real part of the index of refraction $\delta(x_1, x_2, x_3)$. The intensity distribution $I(x, y)$ at a distance $z = d$ and angle of rotation θ is approximated by the following expression, also known as Transport of Intensity equation:[26–29]

$$I^{\theta}_{z=d}(x, y) = I^{\theta}_{z=0}(x, y) - \frac{\lambda d}{2\pi}\nabla_{\perp}\left[I^{\theta}_{z=0}(x, y) \cdot \nabla_{\perp}\phi_{\theta}(x, y)\right] \tag{1}$$

with $\phi_{\theta}(x, y)$ being the phase function of the object. Eq. 1 is valid in the near-field Fresnel region $d \ll a^2/d$, where a is the transversal size of the smallest structure in the object. For a mixed phase-amplitude object with weak and almost homogeneous absorption (i.e. $\frac{\partial \mu_{\theta}}{\partial x}, \frac{\partial \mu_{\theta}}{\partial y} \approx 0$), Eq. 1 simplifies further to:[25]

$$I^{\theta}_{z=d}(x, y) = I^{\theta}_{z=0}(x, y)\left[1 - \frac{\lambda d}{2\pi}\nabla^2\phi_{\theta}(x, y)\right] \tag{2}$$

with $\nabla^2 \equiv \frac{\partial^2}{\partial x^2} + \frac{\partial^2}{\partial y^2}$. The goal of quantitative phase tomography is to reformulate Eq. 2 to obtain $\delta(x_1, x_2, x_3)$ from the knowledge of $I^{\theta}_{z=d}(x, y)$ for $\theta \in [0, \pi]$. Expressing Eq. 2 as $\nabla^2\phi_{\theta}(x, y) = -\frac{2\pi}{\lambda d}g_{\theta}(x, y)$ with $g_{\theta}(x, y) = \frac{I^{\theta}_{z=d}(x,y)}{I^{\theta}_{z=0}(x,y)} - 1$, applying then the 3D Radon transform (denoted by the symbol ˆ), and calculating finally the second derivative with respect to the variable $s = x\cos(\omega) + y\sin(\omega)$ one gets:

$$\frac{\partial^2}{\partial s^2}\hat{\delta}(s, \theta, \omega) = -\frac{1}{d}\hat{g}_{\theta}(s, \omega) \tag{3}$$

Expression 3 is a theorem which states that from the *2D Radon transform* of the measured value g, one can directly find *the 3D Radon transform* of δ.[25] An explicit inversion formula for the 3D Radon transform was given by Radon and Lorentz already at the beginning of the previous century. Combining the 2D Radon transform and its backprojection into a single step one obtains:

$$\delta(x_1, x_2, x_3) = \frac{1}{4\pi d^2}\int_0^{\pi}(q * * g_{\theta})d\theta \tag{4}$$

where the stars indicate a 2D convolution and:

$$q(x, y) := \frac{|y^2|}{x^2 + y^2} \tag{5}$$

This convolution integral can be computed in the Fourier domain by taking the two dimensional Fourier transform. In the Fourier domain, Eq. 5 has the low-pass filter form given by [25]:

$$q(\xi, \eta) = \frac{|\xi|}{\xi^2 + \eta^2} \tag{6}$$

Expressed in this (filtered backprojection) form, see Eq. 4, the approach becomes very interesting since in case of a pure phase object (i.e. $I^{\theta}_{z=0}(x, y) = 1$) the 3D distribution of the refractive index can be recovered from only one single tomographic data set, being:

$$g_{\theta}(x, y) = I^{\theta}_{z=0}(x, y) - 1, \theta \in [0, \pi] \tag{7}$$

This is a significant step since (a) the experimental setup can be kept extremely simple (it is actually the same as for standard, absorption based tomography) and (b) the radiation damage is kept to the minimum, which is of special importance for biological specimens and for potential future in vivo studies. In addition, time consuming data alignment routines as well as phase retrieval processes become superfluous.

3.2.2. Practical implementation - Experimental results

The experimental setup is equivalent to the one for standard absorption tomography. Nevertheless, two additional conditions have to be satisfied: (i) the sample-detector distance (z) is now increased from the minimum ($z = 0$)

used in absorption tomography, to the near field Fresnel region ($z = d$), (ii) the photon energy is increased to maximum attainable (with sufficient flux) at the experimental station† in order to satisfy, as much as possible, the weak and almost homogeneous absorption condition. As a test, we investigated the internal microstructure of 200 microns thin wood samples. Even when low photon energy (10 keV) was used there is a weak absorption contrast and only the edges of internal structures are visible, see Fig. 6(a). In order to apply the phase tomography method in a pure phase object approximation, a single data set $I^{\theta}_{z=d}(x, y))$ of 501 angular projections at a sample detector distance of $z = 32$ mm and at a photon energy of 25 keV was acquired. For the practical implementation of the filter in Eq. 6 a sufficiently small sampling interval has to be used in the frequency domain. This can be achieved by zero padding the discrete data of the experimental function $g_{\theta}(x, y)$. This is a standard technique in digital signal processing to avoid wraparound errors. Fig. 6(b) presents a slice through the sample reconstructed using Eq. 4 and (the filter) 6. The reconstructed slice shown in Fig. 6(b) is severely corrupted by the residual

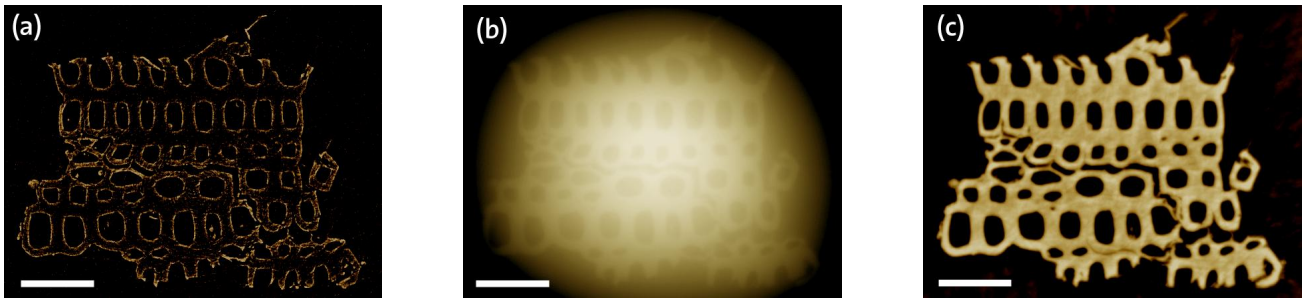

Figure 6. Tomographic reconstruction of a 200 microns thin wood sample: (a) absorbtion contrast at 10 keV, (b) phase contrast, according to Eq. 4 and 6, (c) phase contrast obtained with the MBA. The length of the scale bar is 50 μm, sample courtesy of P. Trtik, ETH Zürich, Switzerland.

absorption artifact (see cap in the center). This means that, even though the absorption level for the wood sample is calculated to be in the range of only 2%, the pure phase object condition is not satisfied and an intensity measurement at zero distance ($I^{\theta}_{z=0}(x, y)$) is also required. Here, we adopted another approach: the reconstruction artifacts are corrected by amending the original method leading to what we named Modified version of Bronnikovs Algorithm (MBA). The correction consists of adding, in the denominator of the low-pass filter given in Eq. 6, an absorption dependent correction factor α_{exp}. Consequently, the new filter becomes:

$$q(\xi, \eta) = \frac{|\xi|}{\xi^2 + \eta^2 + \alpha_{\text{exp}}} \tag{8}$$

The values of α_{exp} to be used are found by using a semi empirical (simulations-experiment) approach, described in details in Ref. [4,5]. Applying the MBA method, we reconstructed again the data set of the wood sample. The result is presented in Fig.6(c). It appears clearly that the absorption artifact has completely disappeared and simple segmentation (global threshold) can be performed. The MBA was validated using the Differential Phase Contrast Imaging technique, see section 3.1 and again Ref. [5]. In general, the two methods are complementary. The full 3D phase imaging approach (MBA) is experimentally simple, very fast and it is ideally suited for small objects when resolution around 1 micron is needed. Deposited dose is equivalent (or lower, since higher photon energy is used) to the one deposited in conventional tomography. The MBA spatial resolution is limited, equivalently to standard absorption tomography, by the detector resolution to around 1 micron.[10] The DPC is more demanding in terms of instrumentation and acquisition time (therefore also deposited dose) but it is more sensitive and can be scaled up to large fields of view. Spatial resolution is limited to two period of analyzer grating[3] e.g. to 2 microns with present fabrication technology.

†For the experiments discussed here, the highest (usable) energy was 25 keV, obtained at the Materials Science beamline 4S of the Swiss Light Source.

4. APPLICATION OF X-RAY TOMOGRAPHIC MICROSCOPY

Synchrotron-based X-ray tomographic microscopy is nowadays an important and powerfool tool for volumetric and nondestructive analysis. This section shows a short palette of basic research currently on-going at the Swiss Light Source. The list is incomplete and by far not exhaustive but should be indicative of what are the current trends in synchrotron-based microtomography. Applications vary from the investigation of fossilized embryos up to the visualization of the brain or bone microvasculature network. All the experiments presented here are carried have been carried out at the tomography station of the SLS,[10] located at the Materials Science beamline[30]

4.1. X-ray tomographic microscopy of fossil embryos

Although only recently discovered, the fossil record of embryonic development has already begun to challenge cherished hypotheses on the origin of major animal groups. Synchrotron-based X-ray Tomographic Microscopy has provided unparalleled insight into the anatomy and preservation of these fossil remains and this has allowed Donoghue et al.[31] to verify competing hypotheses on their nature. With knowledge of both adults and embryos from the time of diversification ($\approx$ 540 million years ago) of the major animals groups, it is now possible to test models of developmental evolution based on modern model organisms using information from their long-extinct ancestors, see Fig. 7.

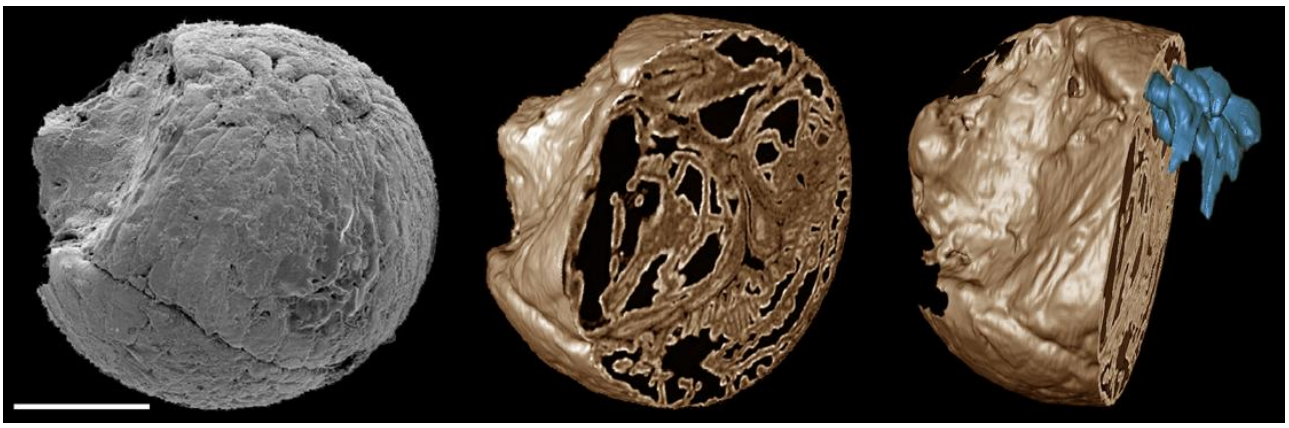

Figure 7. Left: SEM image of an enrolled embryo (head end at upper left; tail end at top). Center: rendered and virtually sectioned to show internal structure. Right: segmented to show the structure of the tail. Scale bar: 150 μm. Image courtesy of P. Donoghue, Bristol University, UK.

4.2. Imaging of the vascular network and osteocytic lacunaes system in cortical bone

Bone strength determination is a crucial point in the worldwide efforts against osteoporosis disease. On a macroscopic scale (0.01-1 mm) bone mass and bone architecture are the dominant parameters determining bone strength. A new hypothesis, proposed by Schneider *et al.*,[32,33] is that ultrastructural (sub-micron) parameters like the bone vascular system and the osteocyte lacunae distribution can sensitively improve the prediction of bone competence. Thanks to a hierarchical imaging approach aimed at the non destructive assessment of these parameters within two distinct murine models, see Fig. 8, it was possible to show that morphometry of these quantitative traits is genetically dependent.

4.3. New insights into lung development

The lungs represent one of the essential, life supporting organs. The current paradigm states (i) that the formation of new alveoli - the formation of new gas-exchange surface - is completed at the age of 2-3 years and (ii) that a later reactivation of this process is not possible anymore. Therefore, a regeneration of lung tissue by a (re)formation of alveoli after any kind of lung injury is also excluded . Schittny *et al.*[34] showed for the first time that (i) alveoli may be formed at any time everywhere in the lung and that (ii) in rats new alveoli are formed as long as the lung is growing. Fig. 9 shows the 3D visualization of the terminal airspaces in a rat lung at different developmental stages.

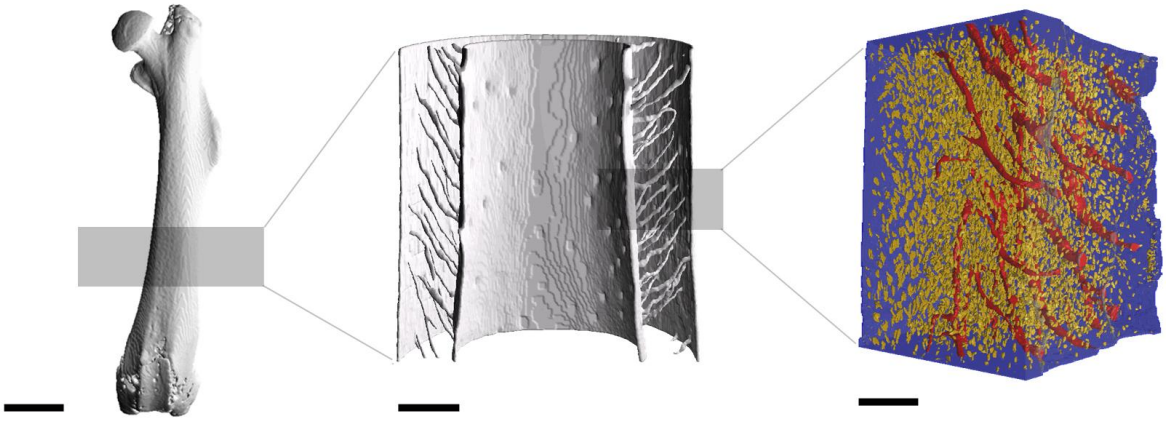

Figure 8. Three different steps of the hierarchical imaging approach introduced by Schneider *et al.*. Left: the whole mouse femur, scanned at low resolution (20 μm) on a tabletop device. Center: High-resolution (3.5 μm) image obtained at the synchrotron showing the vascular network in the cortical bone Right: ultra-high resolution (0.35 μm) showing small details of the vascular network and the distribution of the osteocyte lacunae. The scale bar is 1 mm, 200 microns and 50 microns respectively. Images courtesy of P. Schneider, University and ETH Zürich, Switzerland.

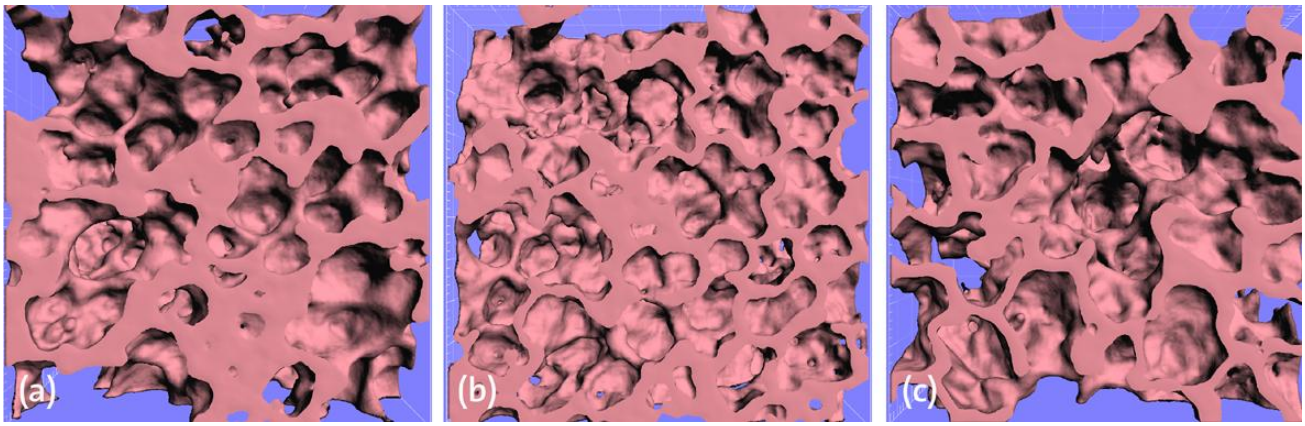

Figure 9. 3D Views of the terminal airspaces of a rat at the age of 10 days (a), 21 (b) and 36 days (c). The alveolarization process is clearly visible. Image courtesy of J. Schittny, University of Bern, Switzerland.

4.4. Multiscale imaging and analysis of the brain microvasculature

There is a wide range of diseases and normal physiological processes that are associated with alterations of the vascular system in organs. Heinzer *et al.*[13] developed a method based on modified vascular corrosion casting (VCC), scanning electron microscopy (SEM) as well as desktop (μCT) and synchrotron radiation (SRμCT) technologies to image vasculature at increasing levels of resolution. This approach allows nondestructive 3D visualization and quantification of large microvascular networks, see Fig. 10, while retaining a precise anatomical context for the region of interest (ROI) scanned at very high resolution. This enables qualitative and quantitative assessment of vasculature at unprecedented resolution and volume with relatively high throughput, opening new possibilities to study vessel architecture and vascular alterations in models of disease.

4.5. Monitoring water flow in soils using X-rays and neutron imaging

Soils are characterized by structures, such as aggregates and fissures, that crucially affect the movement of water, air and solids. Neutron radiography and tomography are efficient tools for real time monitoring of water

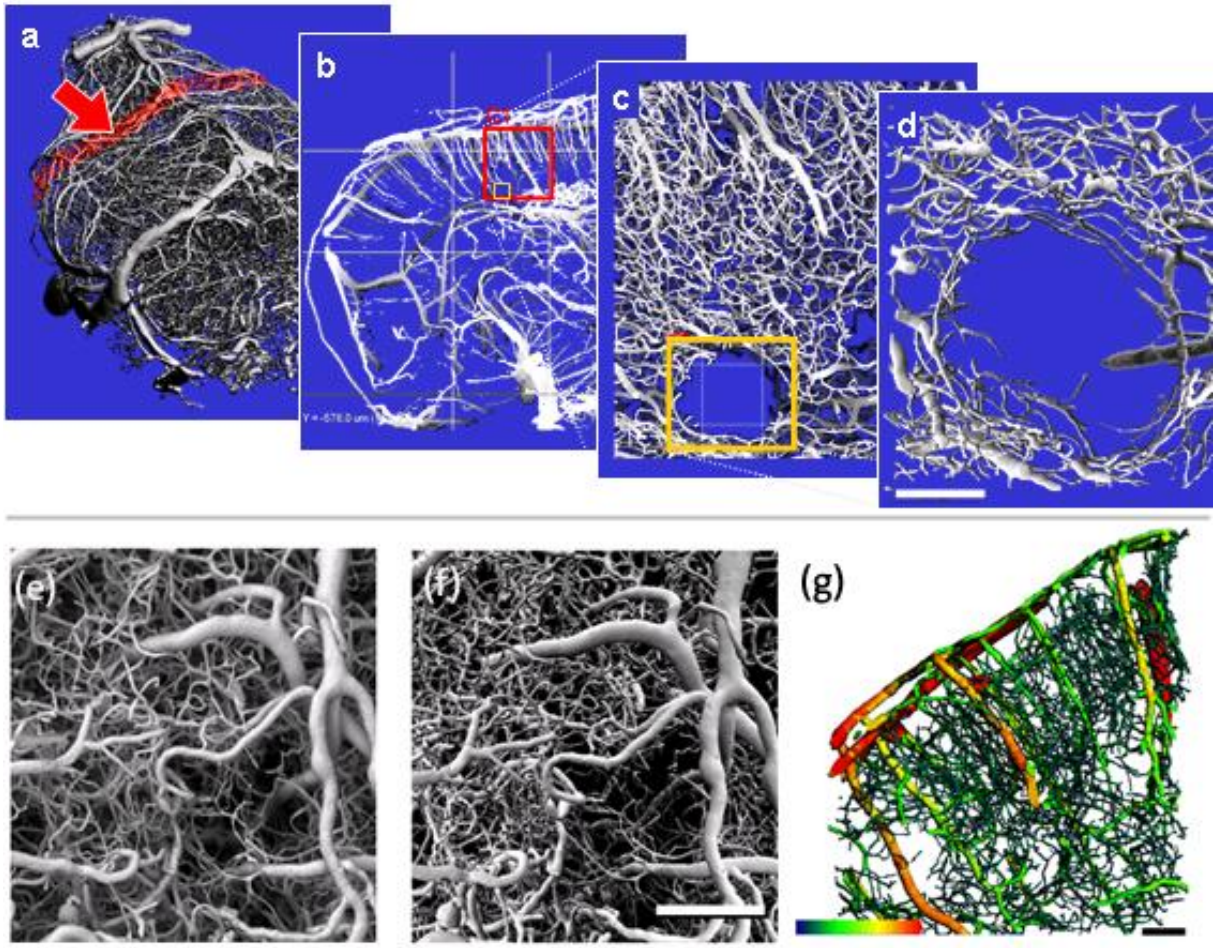

Figure 10. Scans of entire mouse brain VCCs were performed at 16 μm resolution with a desktop μCT system (a-b). Custom-made navigation software with a ROI selection tool enabled the identification of anatomical brain structures and precise placement of multiple ROIs. These were then scanned at 1.4 μm voxel size using SRμCT and a local tomography setup (c-d), scale bar 100 μm. Despite the use of local tomography, exceptional image quality was achieved with SRμCT (f), validated with classical SEM (e), scale bar 200 μm. Full morphometric and topological information can be extracted from the data: here (g), for instance, the vessel thickness of a portion of the left frontal cortex is color-coded from 5 μm (dark gray) to 30 μm (light gray), scale bar: 100 μm. Figures courtesy of S. Heinzer, University and ETH Zürich, Switzerland.

distribution while synchrotron-based X-ray tomography enables to reconstruct the internal fabric of the soil at a resolution of a few microns. By combining the two methods, Carminati *et al.*[35] discovered that micro-heterogeneities control the overall hydraulic behaviour of structured soils. Fig. 11 shows time-series neutron radiographs well illustrating the propagation of the water front. The high-resolution tomography images perfectly visualize the contact between the aggregates.

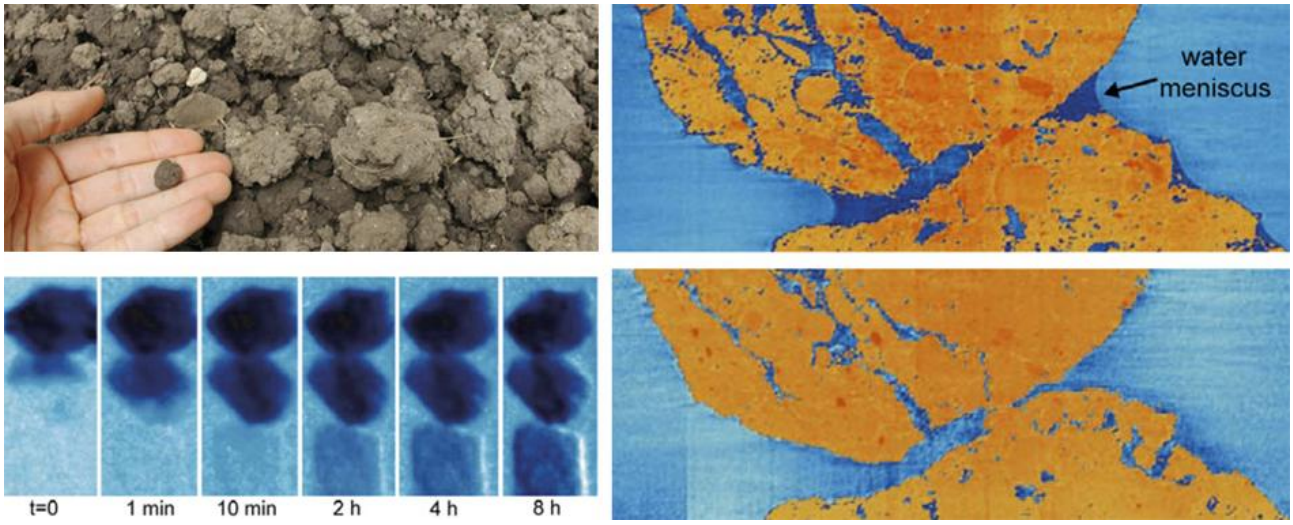

Figure 11. Top left: soil aggregates are structural units frequently observed in top soils. Diameters range from one millimeter to a few centimeters. Bottom left: Time-serises of neturon radiographs. Three aggregates were stacked, forming a sample 5 mm wide and 20 mm long. The initial water input propagates downwards, following gravity and capillary forces. Right: Section of the contact between the aggregates before (top) and after (bottom) drainage. Image courtesy of A. Kaestner, ETH Zürich, Switzerland.

5. ACKNOWLEDGEMENTS

We gratefully acknowledge F. Pfeiffer, O. Bunk, C. David (PSI) and P. Cloetens (ESRF) for the measurements with the grating interferometer at the ESRF.

REFERENCES

1. U. Bonse and M. Hart, "An x-ray interferometer," *Applied Physics Letters.* **6**, pp. 155–157, 1965.
2. P. Cloetens, W. Ludwig, J. Baruchel, D. V. Dyck, J. V. Landuyt, J. P. Guigay, and M. Schlenker, "Holotomography: Quantitative phase tomography with micrometer resolution using hard synchrotron radiation X-rays," *Applied Physics Letters* **75**(19), pp. 2912–2914, 1999.
3. T. Weitkamp, F. Pfeiffer, O. Bunk, A. Diaz, M. Stampanoni, E. Ziegler, P. Cloetens, and C. David, "X-ray phase imaging with a grating interferometer," *Optics Express* **13**, pp. 6296–6304, 2005.
4. A. Groso, P. Schneider, S. Linga, R. Müller, R. Abela, and M. Stampanoni, "Phase contrast tomography: an alternative approach," *Applied Physics Letters* **88**, p. 214104, 2006.
5. A. Groso, R. Abela, and M. Stampanoni, "A fast method for high resolution phase contrast tomography," *Submitted* .
6. F. Pfeiffer, O. Bunk, C. Schulze-Briese, A. Diaz, T. Weitkamp, C. David, J. F. van der Veen, I. Vartanyants, and I. K. Robinson, "Shearing interferometer for quantifying the coherence of hard x-ray beams," *Physical Review Letters* **94**, pp. 164801–4, 2005.
7. U. Bonse and F. Busch, "X-ray computed microtomography (μCT) using synchrotron radiation (SR)," *Progress in Biophysics and Molecular Biology* **65**(1-2), p. 133, 1996.
8. R. Lee, B. Lai, W. Yun, D. C. Mancini, and Z. Cai, "X-ray microtomography as a fast three-dimensional imaging technology using a CCD camera coupled with a $CdWO_4$ single-crystal scintillator," in *Developments in X-Ray Tomography*, U. Bonse, ed., *Proc. SPIE* **3149**, p. 257, 1997.
9. T. Weitkamp, C. Raven, and A. Snigierv, "An imaging and microtomography facility at the ESRF beamline ID 22," in *Developments in X-Ray Tomography II*, U. Bonse, ed., *Proc. SPIE* **3772**, p. 311, 1999.
10. M. Stampanoni, G. L. Borchert, P. Wyss, R. Abela, B. D. Patterson, S. Hunt, D. Vermeulen, and P. Rüegsegger, "High resolution X-ray detector for synchrotron-based microtomography," *Nucl. Intrum. Meth. Phys. Res. A* **491**, pp. 291–301, 2002.

11. S. Nuzzo, F. Peyrin, P. Cloetens, J. Baruchel, and G. Boivin, "Quantification of the degree of mineralization of bone in three dimensions using synchrotron radiation microtomography," *Medical Physics* **29**(11), pp. 2672–2681, 2002.
12. P. Thurner, P. Wyss, R. Voide, M. Stauber, M. Stampanoni, U. Sennhauser, and R. Müller, "Time-lapsed investigation of three-dimensional failure and damage accumulation in trabecular bone using synchrotron light," *Bone* , 2006. In press.
13. S. Heinzer, T. Krucker, M. Stampanoni, R. Abela, E. Meyer, A. Schuler, P. Schneider, and R. Müller, "Hierarchical microimaging for multiscale analysis of large vascular networks," *Neuroimage* , 2006. In press.
14. B. Müller, M. Riedel, and P. Thurner, "Three-dimensional characterization of cell clusters using synchrotron-radiation-based micro-computed tomography," *Microscopy and microanalysis* **12**, pp. 97–105, 2006.
15. R. H. Mathiesen, L. Arnberg, F. Mo, T. Weitkamp, and A. Snigirev, "Time resolved x-ray imaging of dendritic growth in binary alloys," *Physical Review Letters* **83**(24), pp. 5062–5065, 1999.
16. M. Heggli, T. E. amd P. Wyss, P. J. Uggowitzer, and A. A. Gusev, "Approaching representative volume element size in interpenetrating phase composites," *Advanced Engineering Materials* **7**(4), pp. 225–229, 2005.
17. S. Waelchli, P. R. von Rohr, and M. Stampanoni, "Multiphase flow visualization in microchannels using x-ray tomographic microscopy (xtm)," *Journal of Flow Visualization and Image Processing* **12**, pp. 1–13, 2005.
18. A. Momose, T. Takeda, Y. Itai, and K. Hirano, "Phase-contrast X-ray computed tomography for observing biological soft tissues," *Nature Med.* **2**, pp. 473–475, 1996.
19. T. J. Davis, D. Gao, T. E. Gureyev, A. W. Stevenson, and S. W. Wilkins, "Phase-contrast imaging of weakly absorbing materials using hard X-rays," *Nature* **373**, pp. 595–598, 1995.
20. D. Chapman, W. Thomlinson, R. E. Johnston, D. Washburn, E. Pisano, N. Gmür, Z. Zhong, R. Menk, F. Arfelli, and D. Sayers, "Diffraction enhanced x-ray imaging," *Phys. Med. Biol.* **42**, pp. 2015–2025, 1997.
21. S. W. Wilkins, T. E. Gureyev, D. Gao, A. Pogany, and A. W. Stevenson, "Phase-contrast imaging using polychromatic hard x-rays," *Nature* **384**, pp. 335–337, 1996.
22. C. David, B. Nöhammer, H. H. Solak, and E. Ziegler, "Differential x-ray phase contrast imaging using a shearing interferometer," *Applied Physics Letters* **81**(17), pp. 3287–3290, 2002.
23. K. Creath, "Phase-measurement interferometry techniques," in *Progress In Optics XXVI*, E. Wolf, ed., pp. 349–393, Elsevier Science, 1988.
24. A. V. Bronnikov, "Reconstruction formulas in phase-contrast tomography," *Opt. Comm.* **171**, pp. 239–244, 1999.
25. A. V. Bronnikov, "Theory of quantitative phase-contrast computed tomography," *J. Opt. Soc. Am. A* **19**, pp. 472–480, 2002.
26. S. C. Mayo, P. R. Miller, S. W. Wilkins, T. J. Davis, D. Gao, T. E. Gureyev, D. Paganin, D. J. Parry, A. Pogany, and A. W. Stevenson, "Quantitative x-ray projection microscopy: phase-contrast and multi-spectral imaging," *Journal of Microscopy* **207**, pp. 79–96, 2002.
27. L. J. Allen, W. McBride, N. O'Leary, and M. P. Oxley, "Exit wave reconstruction at atomic resolution," *Ultramicroscopy* **100**, pp. 91–104, 2004.
28. W. K. Hsieh, F. R. Chen, J. J. Kai, and A. I. Kirkland, "Resolution extension and exit wave reconstruction in complex hrem," *Ultramicroscopy* **98**, pp. 99–114, 2004.
29. J. M. Cowley, *Diffraction Physics*, North-Holland, Amsterdam, second revised ed., 1981.
30. B. D. Patterson, R. Abela, H. Auderset, Q. Chen, F. Fauth, F. Gozzo, G. Ingold, H. Kühne, M. Lange, D. Maden, D. Meister, P. Pattison, T. Schmidt, B. Schmitt, C. Schulze-Briese, M. Shi, M. Stampanoni, and P. R. Willmott, "The Materials Science Beamline at the Swiss Light Source design and realization," *Nucl. Intrum. Meth. Phys. Res. A* **540**, pp. 42–67, 2005.
31. P. C. J. Donoghue, S.Bengtson, X. Dong, N. J. Gostling, T. Huldtgren, J. A. Cunningham, C. Yin, Z. Yue, F. Peng, and M. Stampanoni, "Synchrotron x-ray tomographic microscopy of fossil embryos," *Nature* , 2006. In press.

32. P. Schneider, M. Stauber, R. Voide, M. Stampanoni, L. R. Donahue, P. Wyss, U. Sennhauser, and R. Müller, "Assessment of murine bone ultrastructure using synchrotron light - towards nano-computed tomography," in *This proceedings*,
33. P. Schneider, M. Stauber, R. Voide, M. Stampanoni, L. R. Donahue, and R. Müller, "Hierarchical micro- and nano-compouted tomography: ultrastructural pheotypes in murine bone of two different inbred mouse strains," *Submitted* .
34. J. C. Schittny, S. I. Mund, and M. Stampanoni, "Local capillary duplication at the basis of newly forming septa allow late alveorization of juvenile and young adult lungs," *Submitted* .
35. A. Carminati, A. Kaestner, P. Lehmann, H. Flühler, E. Lehmann, R. Hassanein, P. Vontobel, M. Stampanoni, and A. Groso, "Monitoring water flow in soils, using neutron and x-ray tomography," *PSI Scientific Report 2005* (1), pp. 28–29.